Bioactive Materials 9 (2022) 92–104

Contents lists available at ScienceDirect

Bioactive Materials

journal homepage: www.sciencedirect.com/journal/bioactive-materials

Electrochemically derived nanographene oxide activates endothelial tip cells and promotes angiogenesis by binding endogenous lysophosphatidic acid

Wenjing Liu [a,b], Haiyun Luo [a], Qinwei Wei [c], Jia Liu [a], Junrong Wu [a], Yanli Zhang [a], Lili Chen [d], Wencai Ren [c], Longquan Shao [a,b,*]

[a] Stomatological Hospital, Southern Medical University, Guangzhou, 510280, China
[b] Guangdong Provincial Key Laboratory of Construction and Detection in Tissue Engineering, Guangzhou, 510515, China
[c] Shenyang National Laboratory for Materials Science, Institute of Metal Research, Chinese Academy of Sciences, Shenyang, 110016, China
[d] Stomatology, Union Hospital, Tongji Medical College, Huazhong University of Science and Technology, Wuhan, 430022, China

ARTICLE INFO

Keywords:
Nanographene oxide
Lysophosphatidic acid
Hydrogen bonding
Endothelial tip cell
Hippo signalling

ABSTRACT

Graphene oxide (GO) exhibits good mechanical and physicochemical characteristics and has extensive application prospects in bone tissue engineering. However, its effect on angiogenesis is unclear, and its potential toxic effects are heavily disputed. Herein, we found that nanographene oxide (NGO) synthesized by one-step water electrolytic oxidation is smaller and shows superior biocompatibility. Moreover, NGO significantly enhanced angiogenesis in calvarial bone defect areas in vivo, providing a good microenvironment for bone regeneration. Endothelial tip cell differentiation is an important step in the initiation of angiogenesis. We verified that NGO activates endothelial tip cells by coupling with lysophosphatidic acid (LPA) in serum via strong hydrogen bonding interactions, which has not been reported. In addition, the mechanism by which NGO promotes angiogenesis was systematically studied. NGO-coupled LPA activates LPAR6 and facilitates the formation of migratory tip cells via Hippo/Yes-associated protein (YAP) independent of reactive oxygen species (ROS) stimulation or additional complex modifications. These results provide an effective strategy for the application of electrochemically derived NGO and more insight into NGO-mediated angiogenesis.

1. Introduction

Angiogenesis prior to bone regeneration and neovascularization is essential for bone engineering because it enables oxygen and nutrient delivery and waste removal and ultimately enhances cellular activity and osteogenesis. Thus, promoting the rapid growth of blood vessels and creating an optimal osteogenic microenvironment is key for successfully reconstructing bone defects. Several recent studies have demonstrated progress in bone reconstruction; however, sufficient vascularization in scaffold-based osteoinductivity remains an important problem that requires an expedient solution [1].

Graphene oxide (GO) is an attractive nanomaterial for stem cell and bone tissue engineering due to its mechanical ductility, biological activity and exceptional physicochemical properties [2,3]. These properties result from the contributions of GO to an environment conducive to the adhesion and proliferation of stem cells and their differentiation towards osteogenic lineages [4,5]. However, the effect of GO on angiogenesis is unclear. Lai reported that bovine serum albumin-capped GO exhibits antiangiogenic effects via ultrastrong vascular endothelial growth factor adsorption [6]. Mukherjee et al. demonstrated that the angiogenic activity of GO at a low concentration is mediated by the production of reactive oxygen species (ROS) and reactive nitrogen species via the activation of endothelial nitric oxide synthase and protein kinase B [7,8]. However, ROS production in target cells is also the main mechanism of its potential cytotoxicity [9]. These discrepancies may be due to differences in the physicochemical characteristics of nanomaterials and biological interactions between GO and specific cell types [10,11]. In addition, the contamination of GO with

Peer review under responsibility of KeAi Communications Co., Ltd.
* Corresponding author. Stomatological Hospital, Southern Medical University, Guangzhou 510280, China Guangdong Provincial Key Laboratory of Construction and Detection in Tissue Engineering, Guangzhou, 510515, China.
E-mail address: shaolongquan@smu.edu.cn (L. Shao).

https://doi.org/10.1016/j.bioactmat.2021.07.007
Received 7 May 2021; Received in revised form 6 July 2021; Accepted 7 July 2021
Available online 13 July 2021

impurities when prepared with the traditional method has an impact on its biological safety. Therefore, a green and improved synthetic strategy is needed to reduce the toxicity of nanomaterials and improve the stability of GO in biological applications.

Angiogenesis is a dynamic and complex process originating in endothelial cells. Under the stimulation of angiogenic factors, activated endothelial tip cells extend filopodia and migrate to induce the sprouting of new blood vessels. Simultaneously, a signal is transmitted to adjacent stalk cells, promoting proliferation and elongation. Moreover, endothelial tip cells can form a lumen by connecting with the tip cell of an adjacent sprouting blood vessel [12]. However, studies on the angiogenic effect of GO are mostly confined to its delivery of relative growth factors and the observation of newly formed blood vessels, and the interaction between GO and endothelial cells has been neglected. Specifically, no related studies regarding the effect and mechanisms involved in the complex process of angiogenesis have been performed.

In this study, we successfully synthesized nanographene oxide (NGO) by novel water electrolytic oxidation to avoid impurity contamination and evaluated the effect of NGO on early angiogenesis in bone defect areas in vivo. Furthermore, in vitro experiments were conducted to uncover the possible mechanism underlying the biological behaviour of human umbilical vein endothelial cells (HUVECs) in response to NGO. This study helps to provide a basis for the biological application of NGO and reveal the effects of its biological interactions on angiogenesis.

2. Methods

2.1. Synthesis and characterization of NGO

The NGO samples were synthesized in the Shenyang National Laboratory for Materials Science as previously described [13]. The details are as follows: A GC panel and a platinum wire were inserted into an electrolytic cell (500 mL) containing 350 mL of diluted H_2SO_4 solution (50 wt%) as the anode and cathode, respectively, and then a constant potential of 3.5 V was applied. After the GC anode was fully oxidized and exfoliated to form a dark yellow solution, a dialysis bag was used to purify ENGO. The dry powders of ENGO were collected by vacuum freeze-drying. The size and morphology were visualized by atomic force microscopy (AFM) (Bruker Dimension edge) and transmission electron microscopy (TEM) (FEI Tecnai G2 f20 s-twin, 200 kV). Characterization by Raman spectroscopy (HORIBA JY LabRAM HR Evolution with 532 nm laser) and X-ray photoelectron spectroscopy (XPS) (Thermo Fisher Scientific K-Alpha with 1486.6 eV) revealed the microstructure and chemical composition of NGO. The functional groups of NGO were further detected by Fourier transform infrared (FTIR) (Bruker VERTEX 80). NGO sheets were suspended in distilled water or endothelial culture medium at a concentration of 0.1 mg/mL for 24 h, after which dynamic light scattering (DLS) analysis and the zeta potential of NGO were assessed using a Zetasizer Nano-ZS (Malvern Instruments, Malvern, UK).

2.2. Preparation of the gelatine methacryloyl (GelMA)/NGO scaffold

The GelMA (EFL-GM-90) used in this work was provided by the Intelligent Manufacturing Research Institute of Suzhou, China [14]. GelMA and NGO were added to PBS at different ratios (0.1 wt%, 0.5 wt %, 1 wt%, 2 wt%, 5 wt% and 10 wt%). Each mixed solution was transferred into a round mould with a diameter of 5 mm and a depth of 1 mm and cured under 405 nm visible light for 10 s.

2.3. Rat model of calvarial bone defects

Eight-week-old male Sprague-Dawley rats were purchased from the Southern Medical University Animal Center and used in the in vivo study. After acclimation to the cages for 1 week, thirty-nine rats were randomly divided into the following four groups (n = 6): control (surgery without GelMA implantation), GelMA (GelMA implantation), NGO/GelMA (implantation of 0.1/0.5/1/2/5/10 wt% NGO/GelMA) and NGO/GelMA + Yes-associated protein (YAP) inhibitor (0.5 wt% NGO/GelMA + 10 μM verteporfin, Selleckchem). Under anaesthesia with sodium pentobarbital, a sizeable calvarial bone defect was created by drilling a 5-mm-diameter trephine burr on the left and right sides. Then, the defect area was filled with the different implants and closed by skin suturing. All procedures were performed under the supervision and approval of the Southern Medical University Ethics and Experimentation Committee (No. L2018157).

2.4. Histological analysis

After two weeks, the rats were euthanized with an overdose of sodium pentobarbital (0.5 mL/kg). The calvarial defect region was harvested, fixed in 4% paraformaldehyde and embedded in paraffin wax. The samples were cut into 5 μm thick serial sections for subsequent histological evaluation. Haematoxylin and eosin (HE) staining and CD31 immunohistochemical assays were performed. Endomucin (Emcn)/CD31 immunofluorescence (IF) staining was performed as follows. Tissues sections were prepared from the groups. A rabbit anti-CD31 antibody (1:100, Bioswamp, China) and rat *anti*-Emcn antibody (1:100, Santa Cruz, USA) were used as the primary antibodies, and FITC-conjugated goat anti-rat IgG (1:200, Proteintech, USA) and goat anti-rabbit IgG-Alexa Fluor® 594 antibodies (1:200, Huabio, China) were used as the secondary antibodies. The stained tissue sections were mounted and imaged by fluorescence microscopy. Angiogenesis was quantified based on the percentage area of Emcn/CD31-positive microvessels in randomly selected fields of view.

2.5. 3D images of newly formed blood vessels

Two weeks after the operation, the rats were anaesthetized with sodium pentobarbital and administered rhodamine B (Sigma, Germany) by angular vein injection. The newly formed blood vessels within 3D images of the area with the bone defect were observed and evaluated based on under two-photon fluorescence microscopy images.

2.6. Cell culture

HUVECs were purchased from Cyagen Biosciences Inc. The cells were cultured in endothelial medium from the EGM-2 Bullet Kit (Lonza, Switzerland) supplemented with 10% foetal bovine serum (FBS) (Gibco, USA) and 1% penicillin/streptomycin (Gibco, USA) in a 5% CO_2 incubator at 37 °C. The cells used for subsequent experiments were between passages three and six.

2.7. Cell proliferation

Cells were seeded in 96-well plates and exposed to NGO at 0, 0.5, 1, 5, 10, 20, 50, 100, 200 or 400 μg/mL for 6, 24, or 48 h. Then, a 10% CCK-8 (Dojindo Laboratories, Kumamoto, Japan) solution was added to each well, and the cells were incubated at 37 °C for 2 h. The absorbance of the supplement solution of each well was measured at 450 nm using a VersaMax microplate reader (Molecular Device, USA).

2.8. Cell cycle progression

The cells were seeded in 6-well plates and exposed to NGO at 0, 1, 5, 20 or 50 μg/mL for 6, 24, or 48 h. The cells were collected and fixed using 70% ethanol overnight before they were stained with propidium (Beyotime, China) and analysed on a flow cytometer (BD FACSAria III, USA) based on labelled DNA.

2.9. Wound healing assay

HUVECs were seeded in 24-well plates. After the cells reached 70%

confluence, a scratch in the wells was made with a sterile pipette tip (1 mL). The nonadherent cells were removed with PBS, and reagents were added according to the appropriate experimental group. The cells were fixed and stained with crystal violet (Leagene, China) after 0 or 16 h. Images were acquired by using a stereomicroscope (Leica, Germany), and gap closure was analysed using ImageJ.

2.10. Tube formation

HUVECs were seeded in a 24-well plate overnight and treated according to the experimental groups. Matrigel (BD Bioscience, USA) was added to a μ-Slide Angiogenesis plate (ibidi, Germany), and the samples were incubated at 37 °C for 30 min. Then, the obtained HUVECs were suspended at 2×10^5/mL and seeded in Matrigel-coated plates. After 3 h, the cells were observed with a BX51 microscope (OLYMPUS, Japan), and the main segment length and numbers of nodes and meshes were also analysed using ImageJ.

2.11. RNA-seq assay

Total RNA was extracted from HUVEC samples exposed to 0 or 5 μg/mL NGO using TRIzol reagent (Invitrogen, USA), and the quantity and purity of the RNA were evaluated. An RNA sequencing library was constructed, and transcriptome sequencing and data analysis were carried out on the Illumina HiSeq platform (OmicStudio, China).

2.12. Reverse transcription-polymerase chain reaction (RT-PCR)

Total RNA was extracted from cells at 70% confluence in the different treatment groups with a RNeasy Mini kit (Foregene Biotec, China); then, the RNA was reverse transcribed (Takara Biotechnology, Japan) according to the manufacturer's instructions. Quantitative PCR was performed with Advanced™ SYBR Green Super Mix (Takara Biotechnology, Japan) according to the manufacturer's protocol. The relative mRNA expression levels of LPAR6, KDR, CD34, DLL4, ID1, ID2, HES1, and NOTCH1 were calculated and normalized to the expression of glyceraldehyde 3-phosphate dehydrogenase (GAPDH).

2.13. Western blotting

Cells were seeded at 1.2×10^6 cells/well in 6-cm wells and treated according to the appropriate experimental group. Cellular protein was extracted from cells at 70% confluence by radioimmunoprecipitation assay lysis buffer (Santa Cruz, USA) from cells at 70% confluence of the cells, and protein concentrations were measured with a BCA protein assay kit (Thermo Scientific, USA). Then, the protein samples from the groups were resolved by sodium dodecyl sulfate-polyacrylamide gel electrophoresis, and the proteins were then transferred to PVDF membranes. The membranes were blocked with 5% BSA in Tris-buffered saline containing 0.1% Tween 20 (TBST) at room temperature for 1 h. The primary antibodies anti-CD34 (1:1000, Santa Cruz, USA), *anti*-DLL4 (1:500, Proteintech, USA), *anti*-KDR (1:1000, Proteintech, USA), *anti*-LPAR6 (1:500, Boster, China), *anti*-RhoA (1:1000, Huabio, China), anti-ROCK1 (1:1000, Huabio, China), *anti*-Lats1 (1:1000, Cell Signaling Technology, USA), *anti*-p-YAP Ser127 (1:1000, Cell Signaling Technology, USA), anti-YAP1 (1:1000, Proteintech, USA) and *anti*-GAPDH (1:1000, Proteintech, USA) were incubated with the membranes overnight at 4 °C. After washing with TBST, the membranes were incubated at room temperature for 1 h with HRP-conjugated anti-rabbit IgG or anti-mouse IgG (1:2000, Cell Signaling Technology, USA). The protein bands were visualized using an enhanced chemiluminescence solution (Millipore, USA).

2.14. Analysis of lysophosphatidic acid (LPA) by ELISA

The solutions were centrifuged at 14,000 rpm for 20 min at 4 °C, and the supernatant was harvested. The LPA level was analysed with an LPA ELISA kit (MEIMIAN, China) according to the manufacturer's protocols. The LPA standard solution (MEIMIAN, China) was prepared with BSA and LPA at a concentration ratio of 3:1. LPA is composed of 20:4/16:0/18:2/18:1/18:0 species with equal concentration. The optical density was recorded by measuring absorbance at a wavelength of 450 nm using a microplate reader (Molecular Devices, USA).

2.15. Preparation of BSA-FITC-labelled NGO

NGO samples and BSA-FITC solution (Solarbio, China) were mixed at a ratio of 1:1 and incubated at 37 °C overnight in the dark. The mixed solutions were centrifuged at 16,000×*g* for 30 min at 4 °C. Finally, BSA-FITC-labelled NGO samples were collected and resuspended in culture medium.

2.16. IF staining

The cells were fixed with 4% paraformaldehyde for 30 min and blocked with 5% BSA for 1 h in the dark. After washing with PBS, the cells were incubated with *anti*-LPAR6 overnight at 4 °C and then goat anti-rabbit IgG-Alexa Fluor® 594 antibody (1:200, Huabio, China) for 1 h at 37 °C. Then, the cells were incubated with a DAPI staining solution (Leagene, China) for 15 min and imaged by laser confocal microscopy (FV10i, Olympus, Japan).

2.17. Detection of cellular ROS

The cells were incubated in 6-well plates and exposed to 0, 1, 5, 20 or 50 μg/mL NGO for 24 h. Cellular ROS levels were assayed after incubation with 10 μM DCFH-DA (Beyotime, China) for 20 min. The measurements were performed with a flow cytometer (BD FACSAria III, USA).

2.18. Molecular dynamic (MD) simulations

The optimization of the geometry of related molecules was performed via the Gaussian 16 package at the level of B3LYP/def2tzvp, and vibration analysis was performed at the same level to ensure that there were no virtual frequencies. An acpepy script was employed to obtain the GAFF force field topology file. Packmol software was used for model construction, and the periodic box was set to $10 \times 10 \times 10$ nm^3. A 30 ns simulation was performed, and the bond length and angle were constrained by the LINCS algorithm. The two-way intercept was set to 1.2 nm, van der Waals interaction, and the long-distance electrostatic interaction was set by the particle-mesh Ewald method.

2.19. Statistical analyses

All data are expressed as the mean ± standard deviation (SD) ($n \geq 3$). Statistical comparisons were carried out using one-way ANOVA or Student's t-test with GraphPad. Differences for which $p < 0.05$ were considered statistically significant.

3. Results and discussion

3.1. Characterization of NGO

In this study, electrolytic oxidation of a glassy carbon anode was used to synthesize NGO as reported previously (Fig. S1a, Supporting Information). AFM and TEM measurements showed that the thickness of NGO was less than 5 nm and the size of most NGO was less than 50 nm (Fig. 1a and b). Raman spectral characterization showed an obvious D peak at 1349 cm^{-1} and a typical G peak at 1588 cm^{-1} from NGO (Fig. 1c), indicating the presence of graphitic sp^2 carbon regions and hybrid structure defects derived from oxygen-containing functional

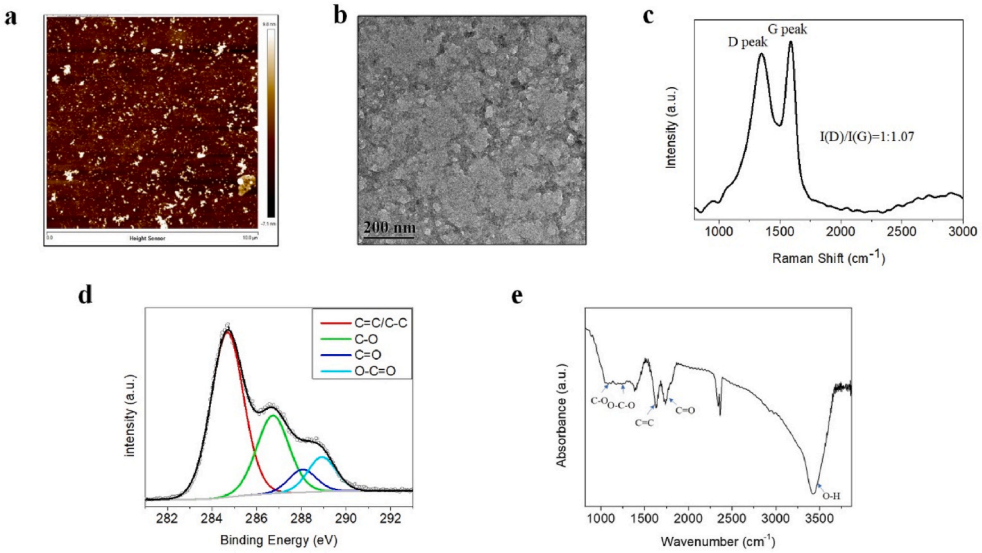

Fig. 1. Characterization of NGO. (a) AFM image of NGO showing the topography and height profile. (b) TEM image of NGO. Scale bar, 200 nm. (c) Raman spectrum of NGO. (d) C 1s XPS spectrum of NGO. (e) FTIR spectrum of NGO.

groups and edges in the NGO sheets. Subsequent XPS spectra showed the presence of the chemical bonds C═C/C–C (284.8 eV), C–O (286.9 eV), and C═O (288.2 eV) and the obvious presence of O–C═O (288.8 eV) in NGO (Fig. 1d). The FTIR spectrum of NGO demonstrated the presence of typical oxygen-containing functional groups, including C–O vibration (1082 cm^{-1}), O–C–O vibration (1254 cm^{-1}), C═C vibration (1630 cm^{-1}), strong C═O vibration (1742 cm^{-1}), and O–H stretching vibration (3424 cm^{-1}) (Fig. 1e). These results confirmed the successful preparation of GO with nanometre dimensions and a high degree of oxidation by electrochemical oxidation. The DLS data indicated that the size of NGO in aqueous solution is 27.34 ± 5.19 nm and that the zeta potential is −60.8 ± 8.60 mV (Figs. S1b and c, Supporting Information), indicating the excellent dispersion of NGO in aqueous solutions [15]. Moreover, NGO also showed strong dispersion stability in cell culture medium (Figs. S1b and c, Supporting Information).

Recently, GO has attracted increasing attention in biomedicine due to its specialized chemical structure, which consists of nanoscale graphitic sp^2 domains, oxidized sp^3 domains and carbon vacancy defects. However, the size of GO sheets usually varies from hundreds of nanometres to a few microns, which is not ideal for in vivo applications [16]. Luo et al. demonstrated that larger GO is more cytotoxic than smaller GO [17]. The term NGO is used to describe GO with smaller lateral dimensions, typically less than 100 nm. Lu et al. also reported that GO with a size of 50 nm is not toxic [18], and this size is similar to the size of the NGO used in the present study. In addition, the large edge-to-area ratio of NGO is enriched in carbonyl and carboxyl groups, which provide a more negative surface charge and superior colloidal stability [13]. These properties were confirmed by the characterization of NGO. Moreover, the physical properties of GO are closely correlated with cell behaviours [19–22]. Electrochemically derived NGO is more hydrophilic and smaller in size than GO, providing a basis for its biological application, which should be further evaluated in detail.

3.2. Angiogenic effect of NGO in vivo

Angiogenesis refers to the formation of new blood vessels from

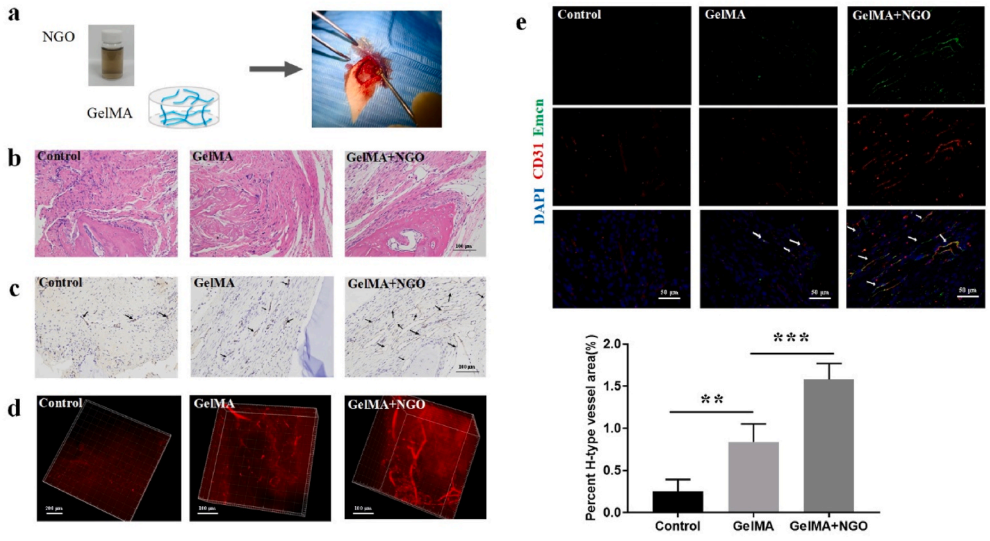

Fig. 2. NGO promoted the formation of new blood vessels in a rat model of calvarial bone defects. (a) NGO/GelMA nanocomposites were implanted into the defect area of rat calvarial bones. (b) HE staining of the defective region in the different groups 2 weeks after implantation. Scale bar, 100 μm. (c) CD31 immunohistochemical staining revealed newly formed blood vessels in the bone defect region 2 weeks after implantation. The results showed optimal lumen formation in the 0.5 wt% NGO/GelMA group (black arrows). Scale bar, 100 μm. (d) 3D images showing angiogenesis in the rat calvarial defect area after 2 weeks indicate adequate support and the best angiogenesis in the defective area in the group treated with the 0.5 wt% NGO/GelMA scaffold. (e) CD31 and Emcn IF staining revealed the presence of newly formed H-type blood vessels in the bone defect region (white arrows); the H-type blood vessel volume was quantified after 2 weeks. Data represent the mean ± SD (n = 6). Scale bars, 50 μm. $^{**}p < 0.005$, $^{***}p < 0.0001$.

existing capillaries and is important for the healing of bone defects. Hence, this study assessed the effects of NGO on early angiogenesis in rats with calvarial bone defects. A GelMA hydrogel was used as a scaffold in the bone defect area. GelMA and NGO/GelMA nanocomposites were implanted into the calvarial bone defect area (Fig. 2a), and the newly formed blood vessels were examined 2 weeks after the operation. The surgical wounds in all rats healed well without oedema or ulcers. No animals died or showed significant body weight changes in the different groups (Fig. S2c). Foreign rejection reactions were not detected in the histological sections. HE staining demonstrated the presence of newly formed typical lumen structures in the defect area in the different groups and a more regular arrangement of connective tissue in the GelMA and NGO/GelMA groups compared with those in the control group, even in scaffolds with higher NGO concentrations (Fig. 2b; Fig. S2a in the supporting information). CD31 immunohistochemical analysis showed an increased number of newly formed blood vessels and greater lumen volume in the 0.5 wt% NGO/GelMA group than in the GelMA and control groups (Fig. 2c; Fig. S2b in the supporting information); this concentration of NGO/GelMA was within the safe ratio for most cell types and from in vivo tissue engineering references [23,24]. Three-dimensional images of blood vessels in the defect regions were obtained using intravenous injection of rhodamine B and multiphoton laser scanning microscopy to offer more intuitive information. The volume of newly formed blood vessels was significantly higher in the 0.5 wt% NGO/GelMA group than in the other two groups. The image also showed that the addition of NGO provided better space support (Fig. 2d).

H-type vessels can be identified by high levels of CD31 and Emcn expression; these vessels have been shown to couple angiogenesis and osteogenesis by regulating osteoblast activity [1]. As expected, the IF staining results showed that the density of $CD31^{hi}Emcn^{hi}$ blood vessels in rat skull bone defects was significantly increased in the 0.5 wt% NGO/GelMA group compared with the GelMA and control groups (Fig. 2e). The percentage area containing H-type blood vessels in the 0.5 wt % NGO/GelMA group was approximately 1.58%, whereas that in the GelMA and control groups was approximately 0.84% and 0.25%, respectively. These results show that more H-type blood vessels were present within the NGO-treated defective areas, which may accelerate new bone regeneration.

As GO fillers impart good mechanical performance and osteoconductivity, they have attracted considerable attention for their application as nanocomposites for bone tissue engineering [25,26]. Angiogenesis precedes osteogenesis, and a large number of osteoprogenitors are recruited and distributed around H-type blood vessels. Previous studies have investigated implanted GO as a delivery system for proangiogenic factors or metal ions to achieve better angiogenesis [27,28]. NGO can maintain ideal stability and is small in size; however, the angiogenic effects of NGO have not been described. GelMA, composed of gelatine and methacrylic anhydride, is similar to the extracellular matrix and has attracted increasing attention in the field of tissue engineering. It has excellent biocompatibility and biodegradability without inductive osteogenesis capacity [29]. The GelMA scaffold complex with NGO was used in the present study to explore the angiogenic effect of NGO in vivo. Our results demonstrated that the appropriate introduction of NGO induced a significant increase in early neovascularization and provided an optimal microenvironment for osteogenesis.

3.3. NGO promoted endothelial tip cell migration and tube formation in vitro

To better understand the intricate regulation of angiogenesis, the potential biological effects of NGO on endothelial cells were further explored in vitro. Initially, the viability of HUVECs was evaluated after incubation with NGO. HUVECs were cultured in the presence of NGO at various concentrations for 6, 24 and 48 h, and the medium was replaced with 10% CCK-8 solution for 2 h. Then, 100 μL of the medium from each well was transferred into a new 96-well plate, and the absorbance was measured. The results indicated no significant difference in HUVEC proliferation between the groups (Fig. 3a). This result is in agreement with the cell cycle detection data, which showed that treatment with NGO at increasing concentrations for 6, 24 and 48 h did not change the ratio of cells in each cell cycle phase (Fig. S3a, Supporting information). Even NGO at the highest concentration tested (400 μg/mL) did not affect the viability of the HUVECs (Fig. 3a). Our findings demonstrate that NGO can be considered a nanomaterial with good biocompatibility.

Activated endothelial cells degrade the basement membrane and migrate towards proangiogenic growth factors, inducing cell assembly and new blood vessel formation (Fig. 3b). Cell migration is an important step during the process of angiogenesis [30]. The migration of HUVECs were cultured in complete endothelial culture medium with 0, 1, 5, 20 and 50 μg/mL NGO was quantified by wound healing assay. The scratch area was visibly reduced after culture in the presence of NGO for 16 h. The wound area upon culture with NGO was smaller than that in the control group, especially in the group stimulated with 5 μg/mL NGO (Fig. 3c), and the wound in this group was nearly 95% healed. The tube formation assay is an effective method for the in vitro assessment and quantification of angiogenesis [1]. NGO promoted the formation of capillary tubes and networks in the tube formation assay. HUVECs were treated with NGO at various concentrations for 24 h, harvested and seeded onto Matrigel for 3 h of incubation. The master segment length and numbers of nodes and formed tube meshes were significantly increased in culture medium treated with NGO compared with the control culture. In particular, these parameters were nearly 2-fold greater in the 5 μg/mL NGO group than in the control group (Fig. 3d). These results suggest that NGO accelerates migration and enhances angiogenesis in endothelial cells.

Endothelial tip cells migrate towards the defect area and connect with the neighbouring tip cells of new sprouts, inducing vascular lumen formation [12]. We next wondered whether accelerated cell migration and tube formation are involved in NGO-mediated endothelial tip cell differentiation. However, the role of NGO in the regulation of sprouting angiogenesis, especially the functions of tip and stalk cells, has not been previously explored. CD34 is an endothelial tip cell marker with high migratory activity [31]. Delta-like ligand4 (DLL4) is expressed at a high level in a vascular endothelial growth factor receptor II (KDR)-dependent extension of filopodia in tip cells [32]. Total RNA was isolated from HUVECs incubated with NGO at various concentrations to identify changes in the expression patterns of these markers. Furthermore, RT-PCR was performed to determine the gene expression profiles of tip and stalk cells. The expression of KDR, DLL4, and CD34 was upregulated in the group treated with NGO at a low concentration (Fig. 3e). Specifically, the mRNA levels of KDR, DLL4, and CD34 were increased 1.5-, 2- and 1.5-fold, respectively, after treatment with 5 μg/mL NGO for 24 h. The stalk cell gene profile, including the ID1, ID2, HES1, and NOTCH1 genes, showed the opposite trend (Fig. 3f). The protein levels of KDR, DLL4, and CD34 in endothelial cells were quantified by western blotting, which showed that the expression of all 3 proteins was approximately 2-fold higher in the group treated with 5 μg/mL NGO for 24 h than in the control group (Fig. 3g; Fig. S3b in supporting information). However, endothelial plasticity during angiogenesis is dynamic and depends on alterations in the microenvironment. DLL4-Notch signalling in the presence of close cell contacts induces tip-stalk switching, which may lead to a change in the cellular bioactivity of NGO with longer treatment times [33]. Our findings demonstrate for the first time that NGO facilitates the endothelial tip cell phenotype during the early stage of sprouting angiogenesis to promote cell migration and sprouting angiogenesis. Thus, 5 μg/mL was selected as the optimal concentration of NGO for subsequent experiments.

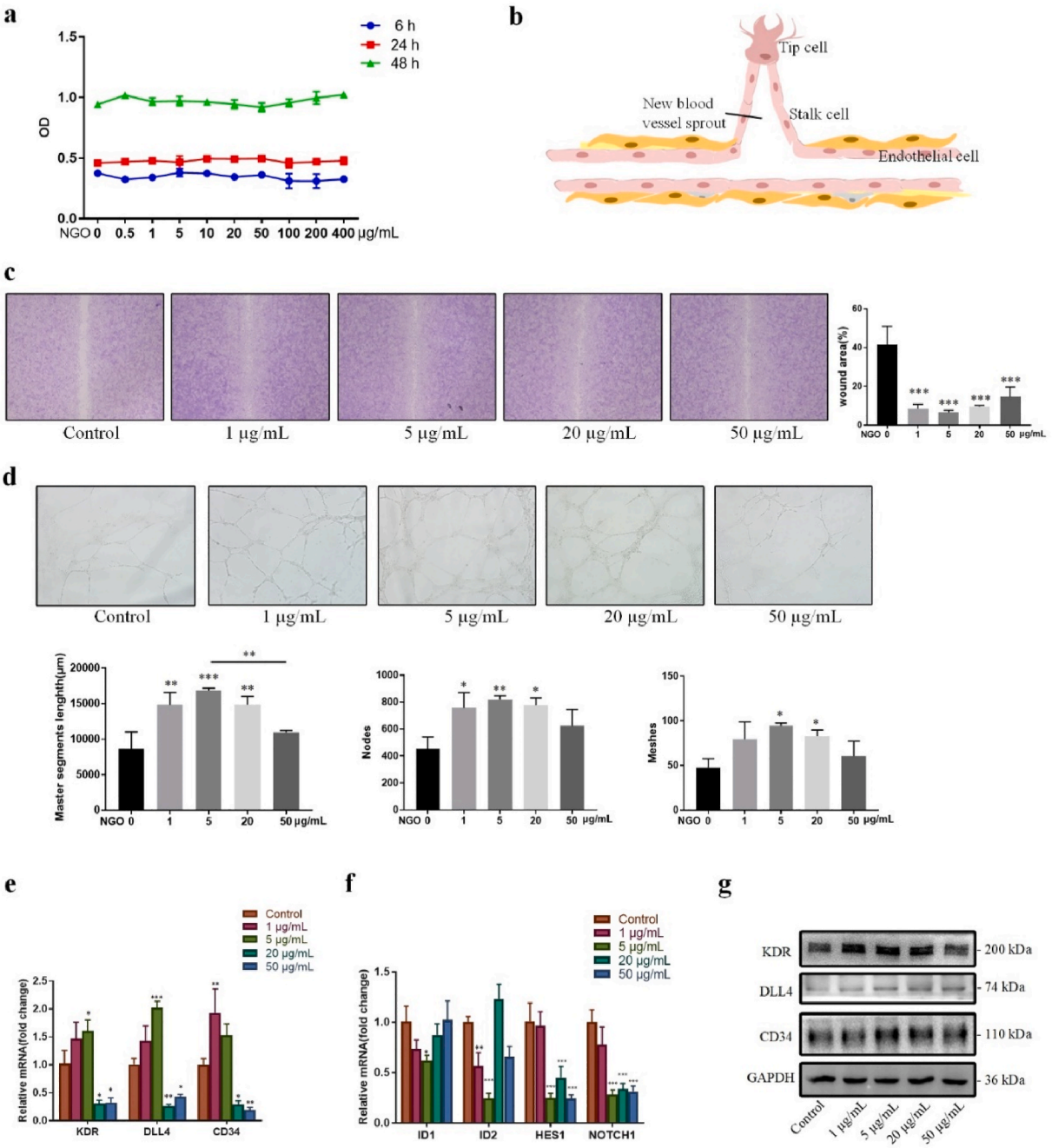

Fig. 3. Effect of NGO on angiogenesis in vitro. (a) HUVECs were incubated in endothelial culture medium (basal endothelial culture medium supplemented with 10% FBS) with NGO at a concentration gradient for 6, 24 and 48 h, and a CCK-8 assay was performed to determine cell viability. (b) Schematic of tip-stalk cell selection in angiogenesis. (c) Wound healing assay in HUVECs cultured in endothelial culture medium with 0, 1, 5, 20 or 50 μg/mL NGO for 16 h. The wound area (%) was measured using ImageJ. (d) Tube formation by HUVECs cultured in endothelial culture medium with 0, 1, 5, 20 or 50 μg/mL NGO for 24 h. The quantified master segment length (μm) and numbers of nodes and meshes are presented in a histogram. (e) The mRNA expression of tip cell-associated genes in HUVECs cultured in endothelial culture medium with 0, 1, 5, 20 or 50 μg/mL NGO for 24 h. (f) The mRNA expression of stalk cell-associated genes in HUVECs treated with 0, 1, 5, 20 or 50 μg/mL NGO for 24 h. (g) Immunoblot detection of KDR, DLL4, and CD34 in HUVECs treated with NGO for 24 h. Data represent the mean ± SD (n = 3). $^{*}p < 0.05$, $^{**}p < 0.005$, $^{***}p < 0.0001$ compared with the control group.

3.4. NGO induced endothelial tip cell formation in HUVECs by binding LPA in the serum

This study further explored the mechanism by which GO activates endothelial tip cells. Previous studies have revealed that GO participates in angiogenesis by regulating ROS production [7]. However, there was no significant difference in ROS production after treatment with NGO (Fig. S4a, Supporting information). This suggests that NGO promotes angiogenesis through other mechanisms. More interestingly, NGO mixed with serum in cell culture medium showed high stability over a long period of time, but the use of basal culture medium without serum as a dispersion solution resulted in a significant increase in the agglomeration and precipitation of NGO (Fig. 4a). These results indicate that serum can promote the stability of NGO in culture medium. Stable dispersion is important for the prospective applications of GO. However, destabilization of GO in the presence of bovine serum due to protein corona formation has been noted as an urgent problem to be solved [34]. In this study, NGO deposits attached to the cell membrane of HUVECs

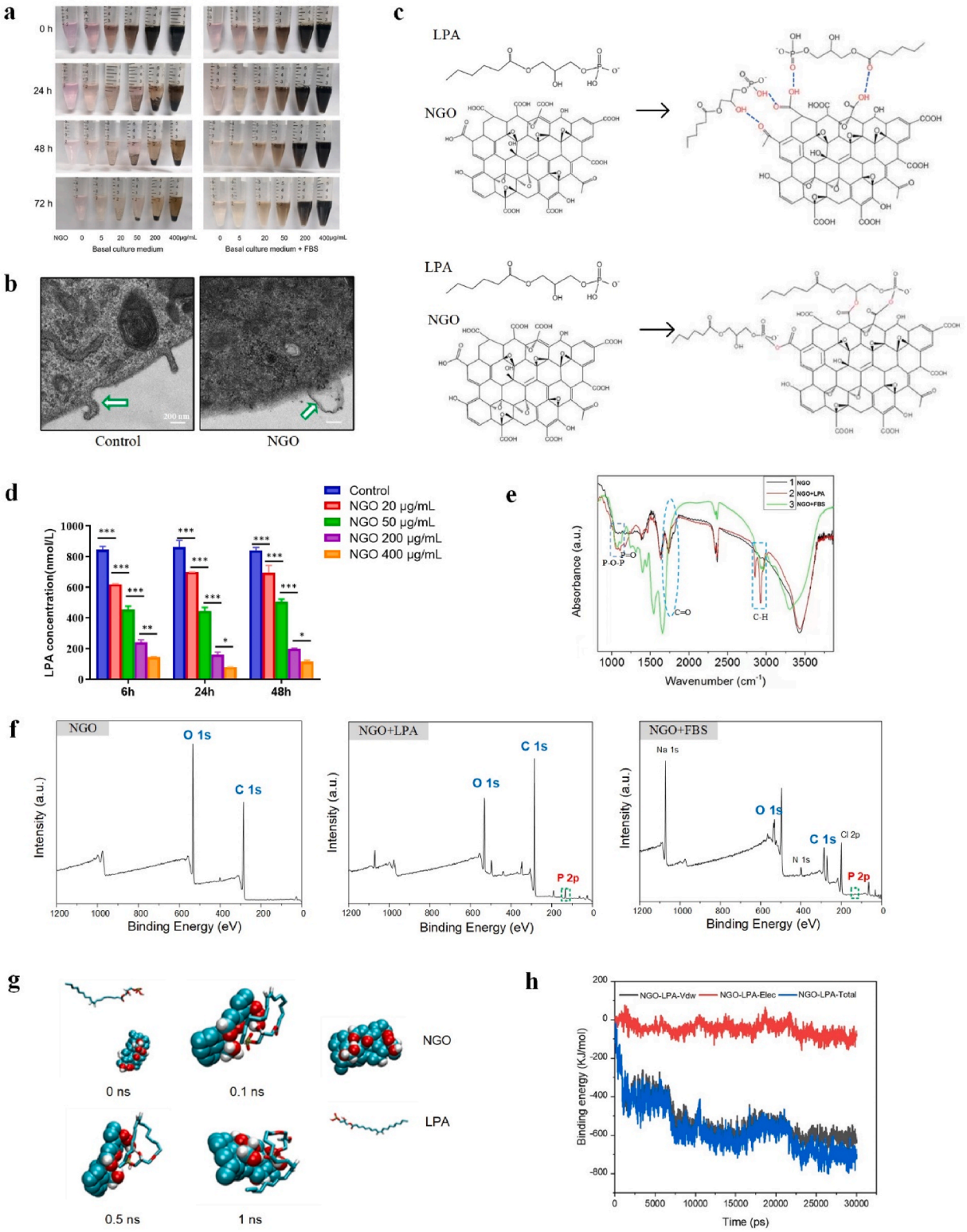

Fig. 4. Characterization of NGO-adsorbed LPA. (a) Images of NGO dispersed in basal culture medium and complete culture medium (basal culture medium + FBS) for 0, 24, 48 and 72 h. (b) TEM images of HUVECs incubated with 5 μg/mL NGO for 24 h at 37 °C; the interface between NGO and the cell membrane is indicated by the white arrow. Scale bars, 200 nm. (c) Schematic illustrations showing the mechanism of NGO loading with LPA. Hydrogen bonds can be formed between NGO and LPA, or esterification reactions may occur. (d) The concentration of LPA in solution after incubation with 20, 50, 200 or 400 μg/mL NGO for 6, 24 or 48 h at 37 °C was measured with an ELISA kit. Error bars are standard deviation across three repetitive experiments. $*p < 0.01$, $**p < 0.001$, $***p < 0.0001$. (e) FTIR analysis demonstrating typical vibrations corresponding to the chemical structure of LPA; the C═O vibration peak in NGO (5 μg/mL) was partially eliminated after incubation in the presence of LPA or FBS for 24 h at 37 °C. (f) XPS analysis showing that the content of P increased in NGO (5 μg/mL) after incubation in the presence of LPA or FBS for 24 h at 37 °C. (g) The self-assembly of NGO and LPA. (h) The binding energy of LPA-NGO during 30 ns simulations. (*Vdw represents van der Waals forces, Elec represents electrostatic interactions and Total represents the total binding energy).

did not include agglomerated material, as shown by TEM detection (Fig. 4b). As reported previously, the smaller size and reduced agglomeration of NGO enabled their cellular internalization relatively easily without causing significant cell damage as reported [34,35]. These data suggest that the biological application of NGO will attract great interest because of the superior cell compatibility and dispersion stability of NGO compared with those of GO and because the use of NGO does not require additional surface modifications or stabilizers.

The excellent dispersibility of GO is facilitated by the formation of strong hydrogen bonds between the functional groups of GO and solvents [36]. LPA is a critical component of serum that consists of a glycerol backbone, an aliphatic acid chain and a phosphate moiety [37]. These characteristics of the molecular structure of LPA suggest that LPA can form hydrogen bonds with the C═O group of NGO and that the carboxyl groups in NGO and hydroxyl groups in LPA may participate in esterification reactions (Fig. 4c). Thus, we hypothesized that LPA plays an important role in the interaction between NGO and serum. To assess our hypothesis, we mixed NGO and LPA and performed multiple experiments. ELISA was used to assess the LPA concentration after the addition of NGO at a concentration gradient. The results showed that LPA levels in the solution were significantly decreased, accompanied by a concomitant increase in the NGO content at various time points, and that the effect was not time-dependent (Fig. 4d). A similar decrease in LPA concentration with a concomitant increase in NGO content was detected when NGO was added to FBS (Fig. S4b, Supporting information). NGO was isolated after coincubation with LPA for 24 h at 37 °C. FTIR spectra showed the presence of functional groups corresponding to the P═O vibration (1224.8 cm^{-1}), P–O–P vibration (1057.0 cm^{-1}) and C–H vibration (2924.0 cm^{-1} and 2852.6 cm^{-1}), in agreement with the chemical structure of LPA [38]. In addition, a reduction in the C═O vibration peak (1737–1741 cm^{-1}) was detected, possibly due to a chemical reaction between the C═O group and hydroxyl group of NGO and LPA, respectively (Fig. 4e). Consistent with the results of FTIR-mediated characterization of NGO treated with LPA, a vibration pattern typical of LPA and similar C═O vibration absorption changes were detected in NGO samples mixed with FBS (Fig. 4e). Further examination by XPS indicated that NGO is mainly composed of the elements C and O. The P/C contents of NGO treated with LPA or FBS increased to 5.36% and 2.43%, respectively, which are higher than those of NGO (0.14%) alone (Fig. 4f). To investigate the self-assembly processes of NGO and LPA in an in-depth manner, we conducted further MD simulations, and the results suggested that the complex of NGO and LPA is easily formed in 0.1 ns and then remains stable (Fig. 4g). Moreover, as shown at 0.5 ns and 1 ns, the hydroxyl groups of NGO and LPA are in close proximity, which suggests that H-bond interactions may play a key role in the binding of NGO and LPA. The binding energy of this system was also studied via MD simulations. As shown inFig. 4h, the binding energy between NGO and LPA is approximately 750 kJ/mol which is relatively stable.

NGO contains epoxy, hydroxyl carbonyl and carboxyl functional groups based on the aromatic ring plane, making these groups available for bioconjugation and endowing NGO with nanocarrier properties [39,40]. Noncovalent and covalent interactions are the most important interactions between NGO and protein molecules. The abundant carboxyl groups in NGO provide a foundation for covalent reactions. Esterification of hydroxy and carboxyl groups is the most likely covalent reaction that occurs between NGO and LPA. Although a change in the C═O vibration peak was also found in the FTIR detection, further studies are needed to determine whether the ester bond is formed. On the other hand, noncovalent interactions between NGO and proteins allow for new biological effects. It has been found that there are noncovalent hydrophobic interactions and van der Waals interactions between the LPA lipophilic “tail” and GO [41,42]. The oxygen-containing functional groups of NGO and LPA also engage in strong noncovalent interactions via hydrogen bonds according to chemical formula analyses. Thus, physical adsorption and hydrogen bonding mainly play an important role in complex stabilization between NGO and LPA. The binding of LPA to NGO can also interfere with the kinetics of lipid extraction between NGO and the cellular membrane [43] and thus plays a key role in alleviating cytotoxicity. These results suggest that NGO can be functionalized with LPA via noncovalent linkages under physiological conditions thus enabling biological applications of NGO and have not been previously reported. However, it is unclear whether NGO promotes endothelial cell angiogenesis by adsorbing LPA in serum.

LPA is a small lipid signalling molecule in the serum and other body fluids. It has a wide range of biological functions and plays an important role in vascular development [44,45]. Thus, we assumed that the binding of local LPA and NGO forms a nanocarrier that accelerates angiogenesis independent of ROS stimulation or additional complex modifications; this assumption had not previously been studied. To further explore the functional effect of LPA in NGO-dependent angiogenesis. Initially, we assessed the concentration of LPA in FBS using ELISA (Figure S4b, Supporting information). Then, an LPA standard solution (60 nmol/L) was added to the basal endothelial culture medium without serum in subsequent experiments. The results of the wound healing experiment clearly showed no significant difference in the wound area between the control and NGO groups cultured in basal endothelial cell medium without LPA. However, the wound area was reduced in response to treatment with NGO plus LPA by approximately 50% compared with that detected upon treatment with NGO or LPA alone (Figure. 5a). The results of the tube formation experiments indicated that the master segment length and numbers of nodes and meshes were significantly greater in the NGO plus LPA group than in the other groups, and there was no obvious difference in these parameters between the control and NGO groups in the absence of LPA (Fig. 5b). Double IF staining for CD34 and DLL4 showed that the number of endothelial tip cells was increased after treatment with NGO plus LPA; however, no significant upregulation was detected after treatment with NGO or LPA alone (Fig. 5c). Consistent with these data, the protein expression levels of the endothelial tip cell-related markers KDR, CD34 and DLL4 were increased 3-, 2- and 2-fold, respectively, in the NGO plus LPA group compared with the group treated with NGO alone (Fig. 5d; Figure S4c in supporting information). These results verified that LPA in FBS is the key mediator by which NGO promotes angiogenesis in vitro.

LPA has been shown to act on endothelial cells and regulate angiogenesis by promoting cell proliferation, migration and tube formation. However, differences in the response to LPA in angiogenesis are likely to depend on cell type and culture conditions [46,47]. Yatomi et al. reported that LPA induces the cytoskeletal reorganization of HUVECs without affecting their proliferation [48], which is in agreement with our results. Furthermore, LPA itself does not induce directional migration in HUVECs, similar to the results in the LPA group observed in the present study. However, the high plasticity of HUVECs enhances their sensitivity to specific conditions, including cell density or signal concentration [46]. Enhanced migration was mediated by LPA plus NGO, possibly due to the interaction of LPA and NGO. The binding of LPA to NGO may change the subtypes and biological activities of LPA, influencing the distribution of LPA within a specific context, and may activate various signalling molecules. Furthermore, the interaction of LPA and NGO upregulated the expression of KDR, DLL4 and CD34 in HUVECs, which resulted in tip cell positioning and proangiogenic sprouting. Thus, the regulatory effect of NGO on angiogenesis may be associated with LPA loading, which has not been reported. Overall, these data highlight the effects of NGO on endothelial tip cell behaviour and provide insights into the biological significance of NGO loading.

3.5. NGO-bound LPA activated endothelial tip cells via the Hippo-YAP signalling pathway

Differences in gene expression in HUVECs exposed to NGO (0 vs. 5 μg/mL for 24 h) were detected using RNA-seq to determine the molecular mechanism of the NGO–cell interaction. The results of gene

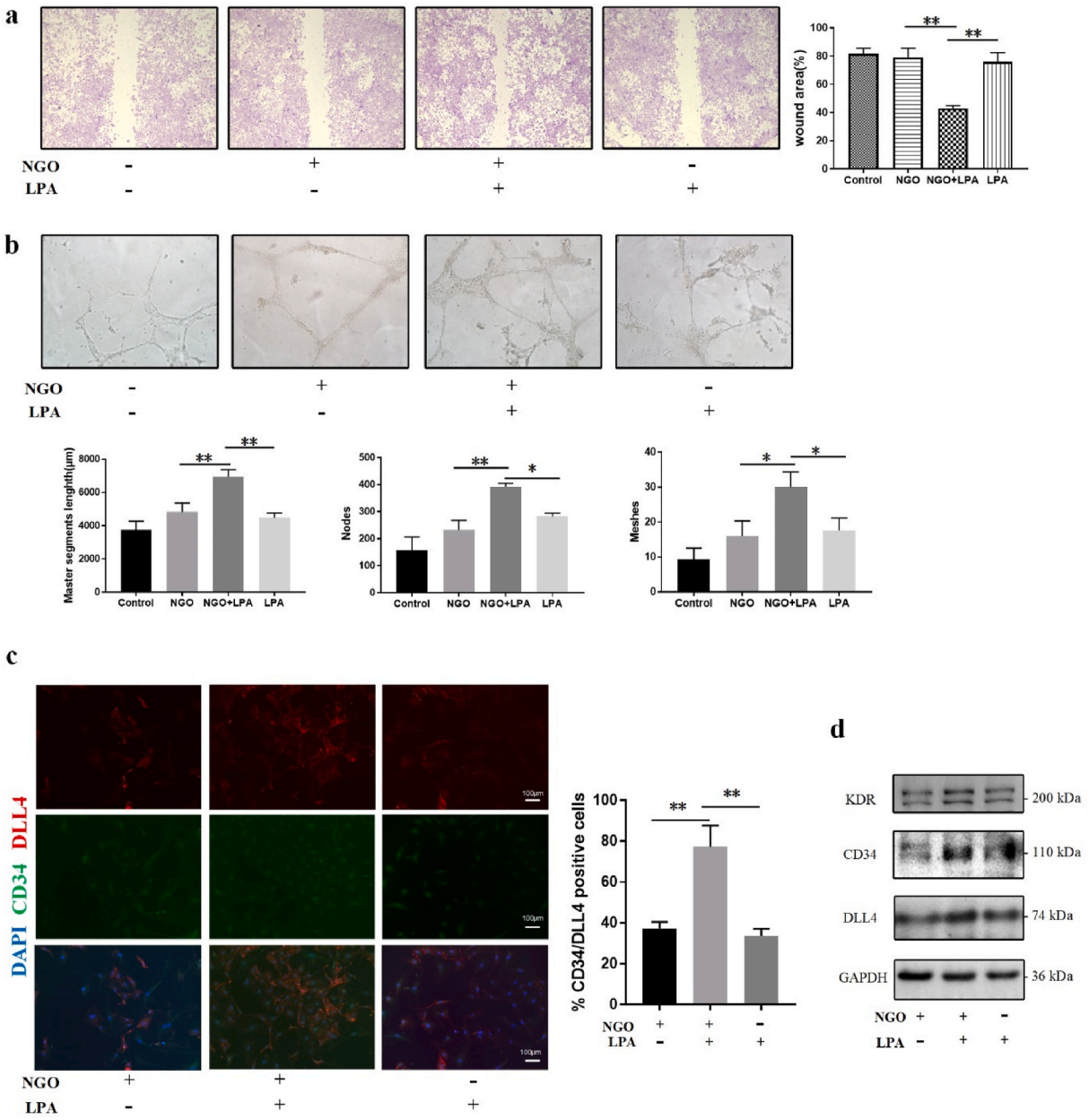

Fig. 5. NGO-adsorbed LPA increased tip cell differentiation. (a) Wound healing assay of HUVECs cultured in basal culture medium without FBS or basal culture medium supplemented with NGO, NGO/LPA or LPA for 24 h. The wound areas (%) in the different groups were subjected to statistical analysis. (b) Tube formation assay in HUVECs cultured in basal culture medium in the absence or presence of NGO, NGO/LPA or LPA for 24 h. The results of quantitative analysis of the master segment length (μm) and numbers of nodes and meshes are presented in a histogram. (c) IF images showing CD34⁻and DLL4-positive cells in the groups. Scale bar, 100 μm. (d) Immunoblot analysis of KDR, CD34, and DLL4 in HUVECs treated with basal culture medium containing NGO, NGO/LPA or LPA for 24 h. Data represent the mean ± SD (n = 3). $*p < 0.05$, $**p < 0.005$.

ontology enrichment analysis showed that certain differentially expressed genes were enriched in the G protein-coupled receptor (GPCR) signalling, angiogenesis and cytoskeleton categories. The Hippo signalling pathway was also enriched in the differentially expressed genes, according to Kyoto Encyclopedia of Genes and Genomes (KEGG) analysis (Fig. 6a, b).

LPA regulates downstream signalling through the GPCRs LPAR1-6, which plays an important role in signal transduction [37]. We detected the expression of different LPA receptors by RT-PCR and confirmed that the gene expression of LPAR6 was increased in the group treated with 5 μg/mL NGO for 24 h compared with the control group (Fig. S5a), which is in agreement with the RNA-seq result (Fig. 6c). The results of laser confocal microscopy indicated that LPAR6 expression was upregulated and coincident with BSA-FITC labelled NGO (Fig. 6d). As shown in MD simulations, the complex of NGO and LPA is stable and became closer together with LPAR6 protein finally (Fig. S6, Supporting information). Moreover, cell migration and tube formation were decreased in the LPAR6-knockdown group with NGO treatment, and the expression of endothelial tip cell-related markers was also down-regulated (Fig. S5c, d, e, f, Supporting information). This result is consistent with the role of LPAR6 in developmental angiogenesis [45, 49]. LPAR6, initially identified as an orphan receptor in 2009 [50], is highly expressed in HUVECs [49]. According to the structure of LPAR6, the ligand-binding pocket and positively charged residues recognize the acyl chain and phosphate head group in the NGO-LPA complex, thus triggering receptor activity [51]. LPAR6 inhibits the activity of adenylyl

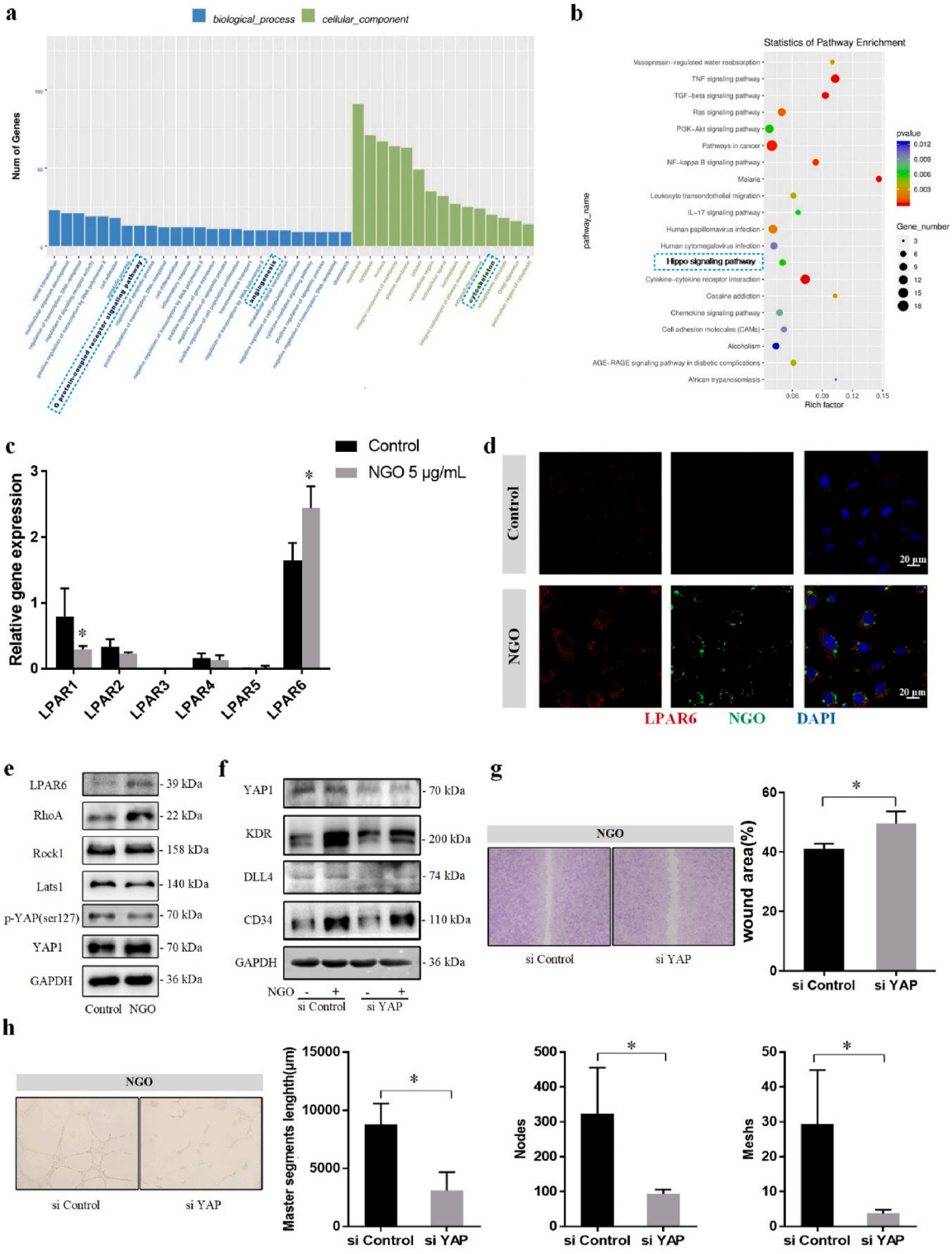

Fig. 6. NGO activates endothelial tip cells via the LPAR6-Hippo-YAP signalling pathway. (a) Gene ontology analysis revealed the enrichment of biological processes, such as cell differentiation, angiogenesis and GPCRs, and cellular components involving the cytoskeleton. (b) The Hippo signalling pathway was enriched in the differentially expressed genes according to KEGG analysis. (c) The mRNA expression levels of LPAR1-6 in HUVECs treated with 0 or 5 μg/mL NGO for 24 h in RNA-seq detection. (d) Laser confocal microscopy showing that LPAR6 expression was upregulated in areas containing BSA-FITC labelled NGO. Scale bar, 20 μm. (e) Protein levels of LPAR6, RhoA, ROCK1, Lats1, p-YAP Ser127 and YAP1 in HUVECs treated with 0 or 5 μg/mL for 24 h were measured by western blotting. (f) Treatment with siRNA targeting YAP (200 nM) caused downregulation of the protein levels of KDR, DLL4, and CD34. (g) Wound healing assay of HUVECs treated with or without siYAP for 24 h in the NGO group. The wound area (%) was measured using ImageJ. (h) A tube formation assay was performed with HUVECs treated with siControl or siYAP and stimulated with NGO for 24 h. Quantitative analysis of the master segment length (μm) and numbers of nodes and meshes in the endothelial network. Data represent the mean ± SD (n = 3). *$p < 0.05$.

cyclase by coupling with the G_i protein, thus reducing the intracellular cAMP content [52]. In addition, LPAR6 binds the $G_{\alpha12/\alpha13}$ protein and subsequently activates the downstream Rho signalling pathway and gene transcription, leading to actin polymerization and promoting cell proliferation and migration [45,49]. NGO treatment was found by gene ontology enrichment analysis to affect the cytoskeleton, which may facilitate filopodia formation and cell migration. Western blot analysis showed that the protein expression of LPAR6, RhoA and ROCK1 was increased in the group treated with 5 μg/mL NGO compared with that in the control group (Fig. 6e; Fig. S5b in supporting information). The involvement of RhoA/ROCK signalling is consistent with a recent report that LPA induces actin stress fibre formation in endothelial cells [49]. This effect in the NGO group was reversed by targeting LPAR6 with siRNAs.

Stress fibre formation does not necessarily induce cell migration. The actomyosin cytoskeleton inhibits Lats1/2, kinases of the Hippo pathway, and thereby induces the nuclear translocation of YAP [53]. YAP is the main mediator of GPCR activity and cell migration and can regulate KDR activity [54]. The RNA-seq results obtained in the present study indicated that YAP1 was one of the significantly upregulated differentially expressed genes in NGO-treated HUVECs compared to control HUVECs. Consistently, the expression of Lats1 and p-YAP Ser127 in HUVECs treated with 5 μg/mL NGO was decreased by one-third compared with that in the control group, and the protein expression of YAP1 was significantly upregulated (Fig. 6e;Fig. S5b in supporting information). Therefore, we hypothesized that YAP plays a key role in NGO-induced endothelial tip cell angiogenesis. To test this hypothesis, RNA interference-mediated silencing of YAP was performed prior to NGO treatment. The protein expression levels of KDR, DLL4 and CD34 were significantly reduced by 26%, 40% and 29%, respectively, in the YAP-knockdown group (Fig. 6f;Fig. S5g in supporting information). The results of the wound healing assay showed that the wound area was larger in HUVECs with YAP knockdown than in siControl-transfected HUVECs (Fig. 6g). Silencing YAP diminished NGO-induced formation of nascent tubes, which was confirmed by a decrease in the master segment length and numbers of nodes and meshes (Fig. 6h). However, the cytoplasmic and nuclear localization of YAP contributes to the growth and integrity of the blood vessel network. During angiogenesis, YAP is mainly localized in the nucleus at the endothelial sprouting area. Mice with conditional knockout of YAP exhibit mild vascular defects [55,56]. Min et al. demonstrated that YAP regulates Dickkopf2 and promotes angiogenesis in rodent and human endothelial cells by regulating filopodial dynamics and angiogenic sprouting [57]. Interestingly, Sakabe et al. demonstrated that cytoplasmic YAP plays an important role in promoting cell migration by activating cell division cycle 42 protein [58]. The difference in these results may be largely due to the status of the cell contacts. Endothelial YAP activity was upregulated when VE-cadherin expression or cell junctions were lost in vitro [56], coincident with the cell density used in our study. Thus, YAP translocation to the nucleus may favours cell migration and rearrangement, further increasing VE-cadherin expression to maintain the junctional integrity required for lumen formation. The data reported in the present study provide new insight into the angiogenic effect of NGO, demonstrating that NGO-bound LPA enhances endothelial tip cell selection and angiogenesis via the LPAR6-Hippo-YAP signalling pathway.

The concentration of NGO nanocomposite optimal for angiogenesis in a rat model of bone defects was determined to be 0.5 wt%, and subsequent studies of the role of YAP in NGO-mediated angiogenesis in vivo were performed at this concentration. In a rat model of calvarial bone defects, the defect regions in the groups treated with the NGO scaffold or NGO scaffold and the YAP inhibitor verteporfin were compared. The number and density of newly formed blood vessels, which were positively stained for CD31, were significantly lower in the verteporfin/NGO group than in the NGO group (Fig. 7a and b). 3D images of blood vessels in the defective site supported the results of the histological analysis (Fig. 7c). Moreover, the formation of H-type blood vessels ($CD31^{hi}Emcn^{hi}$) in the verteporfin/NGO hydrogel scaffold group was significantly reduced by nearly 80% compared with that in the NGO scaffold group (Fig. 7d).

4. Conclusions

Here, we have demonstrated that electrochemically derived NGO has good dispersion stability and biocompatibility. Furthermore, we characterized the interaction between NGO and LPA in physiological fluids and evaluated the underlying mechanisms of their interaction. We found that the binding of NGO with LPA in serum activated LPAR6 and induced endothelial tip cells by Hippo-YAP signalling, facilitating angiogenesis in vitro and in vivo (Fig. 8). In general, our study presents the results of a comprehensive evaluation of the intricate mechanism of

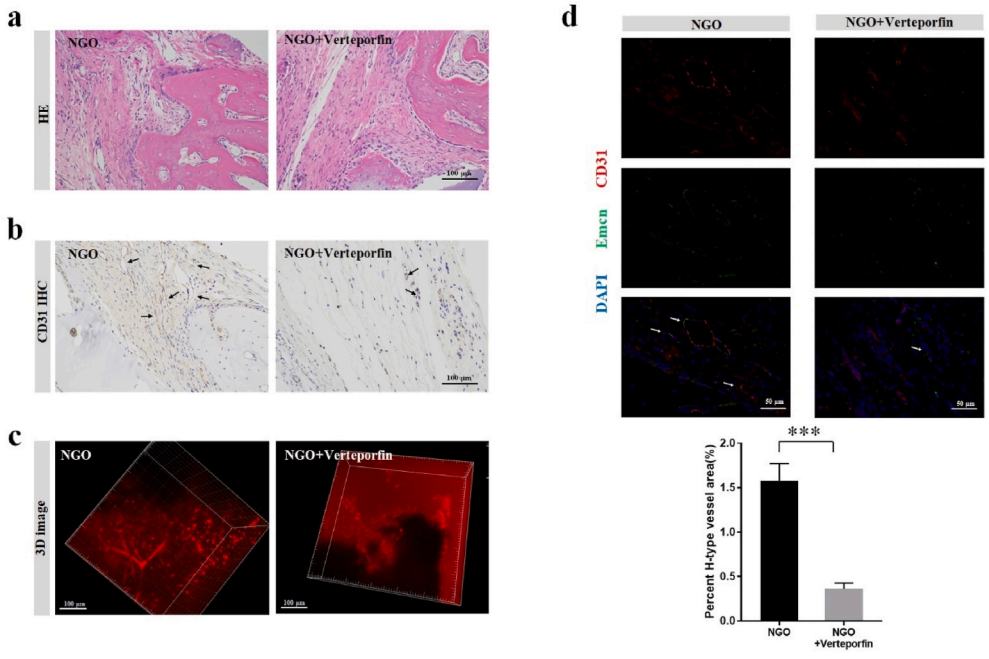

Fig. 7. The role of YAP in NGO-promoted angiogenesis in vivo. (a) HE staining and (b) CD31 immunohistochemical staining of the defective region 2 weeks after implantation in the NGO/GelMA groups with or without the YAP inhibitor verteporfin (10 μM). Scale bar, 100 μm. (c) 3D images of angiogenesis in the area of the calvarial defect 2 weeks after surgery. (d) CD31 and Emcn IF double staining revealing newly formed H-type blood vessels in the bone defect region (Scale bar, 50 μm), and the percentages of H-type blood vessels 2 weeks after surgery in rats treated with or without verteporfin were quantified. Data represent the mean ± SD (n = 6). ***$p < 0.0001$.

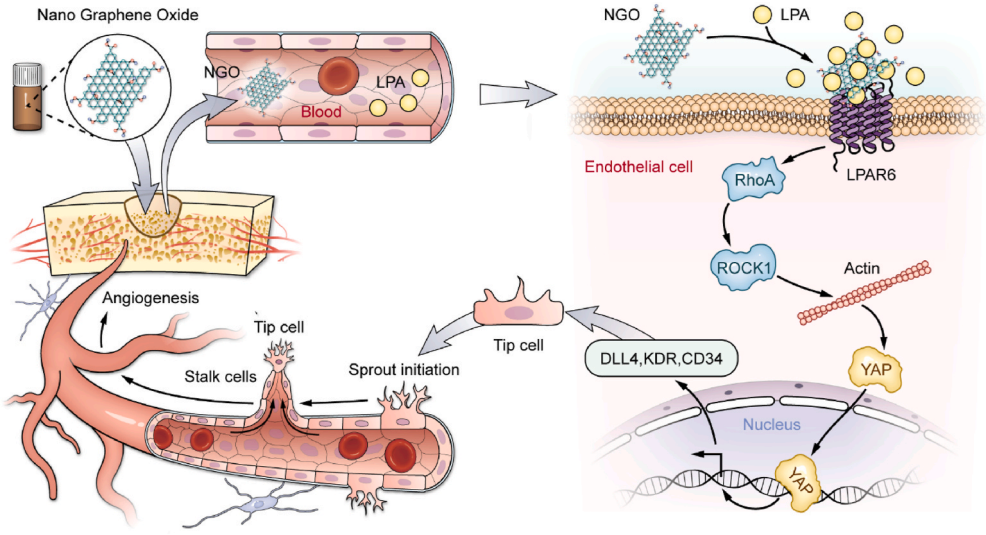

Fig. 8. Schematic representation of the mechanisms by which NGO promotes early angiogenesis at the bone defect site. NGO-bound endogenous LPA induces the nuclear translocation of YAP, thereby activating tip cell specialization and promoting angiogenesis.

angiogenesis regulation. These data provide new information to improve our understanding of how nanomaterials induce biological effects and assist in extending the application of NGO as an ideal modified scaffold for tissue regeneration. Additional in-depth studies of endothelial cell differentiation will provide new ideas for scaffold design.

CRediT authorship contribution statement

Wenjing Liu: Conceptualization, Methodology, Investigation, Formal analysis, Data curation, Writing – original draft, Writing – review & editing. **Haiyun Luo:** Methodology, Investigation, Formal analysis, Writing – review & editing. **Qinwei Wei:** Methodology, Formal analysis, Investigation, Resources, Data curation. **Jia Liu:** Investigation, Data curation, Writing – review & editing. **Junrong Wu:** Investigation, Data curation, Writing – review & editing. **Yanli Zhang:** Investigation, Data curation, Writing – review & editing. **Lili Chen:** Conceptualization, Investigation, Writing – review & editing. **Wencai Ren:** Supervision, Methodology, Resources. **Longquan Shao:** Conceptualization, Supervision, Project administration, Writing – review & editing.

Declaration of competing interest

The authors declare that they have no known competing financial interests or personal relationships that could have appeared to influence the work reported in this paper.

Acknowledgements

This study was supported by the National Natural Science Foundation of China (No. 52072167, 81900989), the Natural Science Foundation of Guangdong Province (2019A1515011980) and the Guangdong Basic and Applied Basic Research Foundation (2019A1515110088).

Appendix A. Supplementary data

Supplementary data to this article can be found online at https://doi.org/10.1016/j.bioactmat.2021.07.007.

References

[1] W.C. Liu, S. Chen, L. Zheng, L. Qin, Angiogenesis assays for the evaluation of angiogenic properties of orthopaedic biomaterials - a general review, Adv healthcare mater 6 (5) (2017).
[2] G. Choe, S. Oh, J.M. Seok, S.A. Park, J.Y. Lee, Graphene oxide/alginate composites as novel bioinks for three-dimensional mesenchymal stem cell printing and bone regeneration applications, Nanoscale 11 (48) (2019) 23275–23285.
[3] T.K. Chang, Y.C. Lu, S.T. Yeh, T.C. Lin, C.H. Huang, C.H. Huang, In vitro and in vivo biological responses to graphene and graphene oxide: a murine calvarial animal study, Int. J. Nanomed. 15 (2020) 647–659.
[4] S.M. Frahs, J.C. Reeck, K.M. Yocham, A. Frederiksen, K. Fujimoto, C.M. Scott, R. S. Beard Jr., R.J. Brown, T.J. Lujan, I.A. Solov'yov, D. Estrada, J.T. Oxford, Prechondrogenic ATDC5 cell attachment and differentiation on graphene foam; modulation by surface functionalization with fibronectin, ACS Appl. Mater. Interfaces 11 (45) (2019) 41906–41924.
[5] H. Fang, C. Luo, S. Liu, M. Zhou, Y. Zeng, J. Hou, L. Chen, S. Mou, J. Sun, Z. Wang, A biocompatible vascularized graphene oxide (GO)-collagen chamber with osteoinductive and anti-fibrosis effects promotes bone regeneration in vivo, Theranostics 10 (6) (2020) 2759–2772.
[6] P.X. Lai, C.W. Chen, S.C. Wei, T.Y. Lin, H.J. Jian, I.P. Lai, J.Y. Mao, P.H. Hsu, H. J. Lin, W.S. Tzou, S.Y. Chen, S.G. Harroun, J.Y. Lai, C.C. Huang, Ultrastrong trapping of VEGF by graphene oxide: anti-angiogenesis application, Biomaterials 109 (2016) 12–22.
[7] S. Mukherjee, P. Sriram, A.K. Barui, S.K. Nethi, V. Veeriah, S. Chatterjee, K. I. Suresh, C.R. Patra, Graphene oxides show angiogenic properties, Advanced healthcare materials 4 (11) (2015) 1722–1732.
[8] C.R. Patra, Graphene oxides and the angiogenic process, Nanomedicine 10 (19) (2015) 2959–2962.
[9] M. Pelin, L. Fusco, C. Martín, S. Sosa, J. Frontiñán-Rubio, J.M. González-Domínguez, M. Durán-Prado, E. Vázquez, M. Prato, A. Tubaro, Graphene and graphene oxide induce ROS production in human HaCaT skin keratinocytes: the role of xanthine oxidase and NADH dehydrogenase, Nanoscale 10 (25) (2018) 11820–11830.
[10] B. Zhang, P. Wei, Z. Zhou, T. Wei, Interactions of graphene with mammalian cells: molecular mechanisms and biomedical insights, Adv. Drug Deliv. Rev. 105 (Pt B) (2016) 145–162.
[11] J. Jeong, H.-J. Cho, M. Choi, W.S. Lee, B.H. Chung, J.-S. Lee, In vivo toxicity assessment of angiogenesis and the live distribution of nano-graphene oxide and its PEGylated derivatives using the developing zebrafish embryo, Carbon 93 (2015) 431–440.
[12] W. Chen, P. Xia, H. Wang, J. Tu, X. Liang, X. Zhang, L. Li, The endothelial tip-stalk cell selection and shuffling during angiogenesis, J cell communication and signaling 13 (3) (2019) 291–301.
[13] Q. Wei, S. Pei, G. Wen, K. Huang, Z. Wu, Z. Liu, W. Ma, H.M. Cheng, W. Ren, High yield controlled synthesis of nano-graphene oxide by water electrolytic oxidation of glassy carbon for metal-free catalysis, ACS Nano 13 (8) (2019) 9482–9490.
[14] L. Shao, Q. Gao, H. Zhao, C. Xie, J. Fu, Z. Liu, M. Xiang, Y. He, Fiber-based Mini tissue with morphology-controllable GelMA microfibers, Small 14 (44) (2018), e1802187.
[15] M.C. Smith, R.M. Crist, J.D. Clogston, S.E. McNeil, Zeta potential: a case study of cationic, anionic, and neutral liposomes, Anal. Bioanal. Chem. 409 (24) (2017) 5779–5787.
[16] M. Zhang, T. Okazaki, Y. Iizumi, E. Miyako, R. Yuge, S. Bandow, S. Iijima, M. Yudasaka, Preparation of small-sized graphene oxide sheets and their biological applications, J. Mater. Chem. B 4 (1) (2016) 121–127.
[17] Y. Luo, X. Wang, Y. Cao, Transcriptomic analysis suggested the involvement of impaired lipid droplet biogenesis in graphene oxide-induced cytotoxicity in human umbilical vein endothelial cells, Chem. Biol. Interact. 333 (2021) 109325.

[18] P. Lu, A. Zehtab Yazdi, X.X. Han, K. Al Husaini, J. Haime, N. Waye, P. Chen, Mechanistic insights into the cytotoxicity of graphene oxide derivatives in mammalian cells, Chem. Res. Toxicol. 33 (9) (2020) 2247–2260.
[19] E.S. Kang, I. Song, D.S. Kim, U. Lee, J.K. Kim, H. Son, J. Min, T.H. Kim, Size-dependent effects of graphene oxide on the osteogenesis of human adipose-derived mesenchymal stem cells, Colloids Surf. B Biointerfaces 169 (2018) 20–29.
[20] G. Reina, N.D.Q. Chau, Y. Nishina, A. Bianco, Graphene oxide size and oxidation degree govern its supramolecular interactions with siRNA, Nanoscale 10 (13) (2018) 5965–5974.
[21] Y. Luo, J. Peng, C. Huang, Y. Cao, Graphene oxide size-dependently altered lipid profiles in THP-1 macrophages, Ecotoxicol. Environ. Saf. 199 (2020) 110714.
[22] J. Ma, R. Liu, X. Wang, Q. Liu, Y. Chen, R.P. Valle, Y.Y. Zuo, T. Xia, S. Liu, Crucial role of lateral size for graphene oxide in activating macrophages and stimulating pro-inflammatory responses in cells and animals, ACS Nano 9 (10) (2015) 10498–10515.
[23] D. Mohammadrezaei, H. Golzar, M. Rezai Rad, M. Omidi, H. Rashedi, F. Yazdian, A. Khojasteh, L. Tayebi, In vitro effect of graphene structures as an osteoinductive factor in bone tissue engineering: a systematic review, J. Biomed. Mater. Res. 106 (8) (2018) 2284–2343.
[24] G.M. Vlasceanu, A. Șelaru, S. Dinescu, C. Balta, H. Herman, S. Gharbia, A. Hermenean, M. Ionita, M. Costache, Comprehensive appraisal of graphene-oxide ratio in porous biopolymer hybrids targeting bone-tissue regeneration, Nanomaterials 10 (8) (2020).
[25] J. Zhang, H. Eyisoylu, X.H. Qin, M. Rubert, R. Müller, 3D bioprinting of graphene oxide-incorporated cell-laden bone mimicking scaffolds for promoting scaffold fidelity, osteogenic differentiation and mineralization, Acta Biomater. 121 (2021) 637–652.
[26] H. Elkhenany, S. Bourdo, S. Hecht, R. Donnell, D. Gerard, R. Abdelwahed, A. Lafont, K. Alghazali, F. Watanabe, A.S. Biris, D. Anderson, M. Dhar, Graphene nanoparticles as osteoinductive and osteoconductive platform for stem cell and bone regeneration, Nanomed. Nanotechnol. Biol. Med. 13 (7) (2017) 2117–2126.
[27] W. Zhang, Q. Chang, L. Xu, G. Li, G. Yang, X. Ding, X. Wang, D. Cui, X. Jiang, Graphene oxide-copper nanocomposite-coated porous CaP scaffold for vascularized bone regeneration via activation of hif-1α, Advanced healthcare materials 5 (11) (2016) 1299–1309.
[28] A. Paul, A. Hasan, H.A. Kindi, A.K. Gaharwar, V.T. Rao, M. Nikkhah, S.R. Shin, D. Krafft, M.R. Dokmeci, D. Shum-Tim, A. Khademhosseini, Injectable graphene oxide/hydrogel-based angiogenic gene delivery system for vasculogenesis and cardiac repair, ACS Nano 8 (8) (2014) 8050–8062.
[29] W.H. Wang, F. Wang, H.F. Zhao, K. Yan, C.L. Huang, Y. Yin, Q. Huang, Z.Z. Chen, W.Y. Zhu, Injectable magnesium-zinc alloy containing hydrogel complex for bone regeneration, Frontiers bioeng biotechno 8 (2020) 617585.
[30] L. Lamalice, F. Le Boeuf, J. Huot, Endothelial cell migration during angiogenesis, Circ. Res. 100 (6) (2007) 782–794.
[31] M.G. Dallinga, B. Yetkin-Arik, R.P. Kayser, I.M.C. Vogels, P. Nowak-Sliwinska, A. W. Griffioen, C.J.F. van Noorden, I. Klaassen, R.O. Schlingemann, IGF2 and IGF1R identified as novel tip cell genes in primary microvascular endothelial cell monolayers, Angiogenesis 21 (4) (2018) 823–836.
[32] A. Benn, C. Hiepen, M. Osterland, C. Schütte, A. Zwijsen, P. Knaus, Role of bone morphogenetic proteins in sprouting angiogenesis: differential BMP receptor-dependent signaling pathways balance stalk vs. tip cell competence, Faseb. J. : off publ Federation Am Soc Experimental Biology 31 (11) (2017) 4720–4733.
[33] M.E. Pitulescu, I. Schmidt, B.D. Giaimo, T. Antoine, F. Berkenfeld, F. Ferrante, H. Park, M. Ehling, D. Biljes, S.F. Rocha, U.H. Langen, M. Stehling, T. Nagasawa, N. Ferrara, T. Borggrefe, R.H. Adams, Dll4 and Notch signalling couples sprouting angiogenesis and artery formation, Nat. Cell Biol. 19 (8) (2017) 915–927.
[34] G. Reina, A. Ruiz, D. Murera, Y. Nishina, A. Bianco, "Ultramixing": a simple and effective method to obtain controlled and stable dispersions of graphene oxide in cell culture media, ACS Appl. Mater. Interfaces 11 (8) (2019) 7695–7702.
[35] C. Wu, C. Wang, T. Han, X. Zhou, S. Guo, J. Zhang, Insight into the cellular internalization and cytotoxicity of graphene quantum dots, Advanced healthcare materials 2 (12) (2013) 1613–1619.
[36] J. Chen, F. Dai, L. Zhang, J. Xu, W. Liu, S. Zeng, C. Xu, L. Chen, C. Dai, Molecular insights into the dispersion stability of graphene oxide in mixed solvents: theoretical simulations and experimental verification, J. Colloid Interface Sci. 571 (2020) 109–117.
[37] Y. Zhao, S. Hasse, C. Zhao, S.G. Bourgoin, Targeting the autotaxin - lysophosphatidic acid receptor axis in cardiovascular diseases, Biochem. Pharmacol. 164 (2019) 74–81.
[38] J.H. Choi, H. Jeon, J.E. Song, J.M. Oliveira, R.L. Reis, G. Khang, Biofunctionalized lysophosphatidic acid/silk fibroin film for cornea endothelial cell regeneration, Nanomaterials 8 (5) (2018).
[39] G. Gonçalves, M. Vila, M.T. Portolés, M. Vallet-Regi, J. Gracio, P.A. Marques, Nano-graphene oxide: a potential multifunctional platform for cancer therapy, Advanced healthcare materials 2 (8) (2013) 1072–1090.
[40] K. Yang, L. Feng, X. Shi, Z. Liu, Nano-graphene in biomedicine: theranostic applications, Chem. Soc. Rev. 42 (2) (2013) 530–547.
[41] X. Chen, W. Gui, H. Liu, Q. Ma, A novel CuZnInS quantum dot-based ECL sensing system for lysophosphatidic acid detection, Analyst 142 (21) (2017) 4142–4149.
[42] S.J. Liu, Q. Wen, L.J. Tang, J.H. Jiang, Phospholipid-graphene nanoassembly as a fluorescence biosensor for sensitive detection of phospholipase D activity, Anal. Chem. 84 (14) (2012) 5944–5950.
[43] X. Zhang, F. Cao, L. Wu, X. Jiang, Understanding the synergic mechanism of weak interactions between graphene oxide and lipid membrane leading to the extraction of lipids, Langmuir : the ACS journal of surfaces and colloids 35 (43) (2019) 14098–14107.
[44] Y. Hisano, T. Hla, Bioactive lysolipids in cancer and angiogenesis, Pharmacol. Ther. 193 (2019) 91–98.
[45] D. Yasuda, D. Kobayashi, N. Akahoshi, T. Ohto-Nakanishi, K. Yoshioka, Y. Takuwa, S. Mizuno, S. Takahashi, S. Ishii, Lysophosphatidic acid-induced YAP/TAZ activation promotes developmental angiogenesis by repressing Notch ligand Dll4, J. Clin. Invest. 129 (10) (2019) 4332–4349.
[46] Y. Chen, D.P. Ramakrishnan, B. Ren, Regulation of angiogenesis by phospholipid lysophosphatidic acid, Front. Biosci. 18 (2013) 852–861.
[47] A. Kazlauskas, Lysophosphatidic acid contributes to angiogenic homeostasis, Exp. Cell Res. 333 (2) (2015) 166–170.
[48] Y. Yatomi, T. Ohmori, G. Rile, F. Kazama, H. Okamoto, T. Sano, K. Satoh, S. Kume, G. Tigyi, Y. Igarashi, Y. Ozaki, Sphingosine 1-phosphate as a major bioactive lysophospholipid that is released from platelets and interacts with endothelial cells, Blood 96 (10) (2000) 3431–3438.
[49] H. Yukiura, K. Kano, R. Kise, A. Inoue, J. Aoki, LPP3 localizes LPA6 signalling to non-contact sites in endothelial cells, J. Cell Sci. 128 (21) (2015) 3871–3877.
[50] J. Chun, T. Hla, K.R. Lynch, S. Spiegel, W.H. Moolenaar, International union of basic and clinical pharmacology. LXXVIII. Lysophospholipid receptor nomenclature, Pharmacol. Rev. 62 (4) (2010) 579–587.
[51] R. Taniguchi, A. Inoue, M. Sayama, A. Uwamizu, K. Yamashita, K. Hirata, M. Yoshida, Y. Tanaka, H.E. Kato, Y. Nakada-Nakura, Y. Otani, T. Nishizawa, T. Doi, T. Ohwada, R. Ishitani, J. Aoki, O. Nureki, Structural insights into ligand recognition by the lysophosphatidic acid receptor LPA(6), Nature 548 (7667) (2017) 356–360.
[52] S.M. Pasternack, I. von Kügelgen, K. Al Aboud, Y.A. Lee, F. Rüschendorf, K. Voss, A. M. Hillmer, G.J. Molderings, T. Franz, A. Ramirez, P. Nürnberg, M.M. Nöthen, R. C. Betz, G protein-coupled receptor P2Y5 and its ligand LPA are involved in maintenance of human hair growth, Nat. Genet. 40 (3) (2008) 329–334.
[53] T. Azad, M. Ghahremani, X. Yang, The role of YAP and TAZ in angiogenesis and vascular mimicry, Cells 8 (5) (2019).
[54] F.X. Yu, B. Zhao, N. Panupinthu, J.L. Jewell, I. Lian, L.H. Wang, J. Zhao, H. Yuan, K. Tumaneng, H. Li, X.D. Fu, G.B. Mills, K.L. Guan, Regulation of the Hippo-YAP pathway by G-protein-coupled receptor signaling, Cell 150 (4) (2012) 780–791.
[55] F. Neto, A. Klaus-Bergmann, Y.T. Ong, S. Alt, A.C. Vion, A. Szymborska, J. R. Carvalho, I. Hollfinger, E. Bartels-Klein, C.A. Franco, M. Potente, H. Gerhardt, YAP and TAZ regulate adherens junction dynamics and endothelial cell distribution during vascular development, eLife 7 (2018).
[56] H.J. Choi, H. Zhang, H. Park, K.S. Choi, H.W. Lee, V. Agrawal, Y.M. Kim, Y. G. Kwon, Yes-associated protein regulates endothelial cell contact-mediated expression of angiopoietin-2, Nat. Commun. 6 (2015) 6943.
[57] J.K. Min, H. Park, H.J. Choi, Y. Kim, B.J. Pyun, V. Agrawal, B.W. Song, J. Jeon, Y. S. Maeng, S.S. Rho, S. Shim, J.H. Chai, B.K. Koo, H.J. Hong, C.O. Yun, C. Choi, Y. M. Kim, K.C. Hwang, Y.G. Kwon, The WNT antagonist Dickkopf2 promotes angiogenesis in rodent and human endothelial cells, J. Clin. Invest. 121 (5) (2011) 1882–1893.
[58] M. Sakabe, J. Fan, Y. Odaka, N. Liu, A. Hassan, X. Duan, P. Stump, L. Byerly, M. Donaldson, J. Hao, M. Fruttiger, Q.R. Lu, Y. Zheng, R.A. Lang, M. Xin, YAP/TAZ-CDC42 signaling regulates vascular tip cell migration, Proc. Natl. Acad. Sci. U. S.A. 114 (41) (2017) 10918–10923.